AIAA-2021-2004

Control of Flow Separation Over a Curved Surface using Fluidic Actuator Arrays with Variable Spanwise Periodicity

Curtis J. Peterson[1], Bojan Vukasinovic[2], Marilyn J. Smith[3] and Ari Glezer[4]

Woodruff School of Mechanical Engineering, Georgia Institute of Technology, Atlanta, GA 30332-0405, USA.

Control of a separation cell that forms in the cross flow over a nominally 2-D curved surface that models the suction surface of a VR-12 airfoil is investigated experimentally in a small-scale transonic wind tunnel. Actuation is effected by exploiting the unsteady interactions between spanwise arrays of fluidic oscillating jets of varying periodicity and vorticity concentrations within the separation cell. The effect of these interactions on the topology of the separated flow and its ultimate reattachment are investigated using high-resolution stereo particle image velocimetry with specific emphasis on the evolution of spanwise distributions and characteristic scales of engendered streamwise vorticity concentrations. The time-averaged flow exhibits nominally spanwise-periodic coupled counter-rotating streamwise vorticity concentrations whose spanwise wavelength and characteristic cross stream scale are commensurate with the periodicity of the actuation jets. It is remarkable that the unsteady shear flow associated with the actuation jets leads to the formation of multiple strands of small-scale streamwise vorticity concentrations of alternating signs within each of the "cores" of the time-averaged single-sense vortices. The streamwise vortical structures are accompanied by spanwise-alternating upwash and downwash regions between and along the axes of neighboring actuation jets, respectively, that lead to the formation of high and low concentrations of turbulent kinetic energy (TKE) as the advected vortical structures stretch into the cross flow. Surface oil visualization shows that the actuation divides the central domain of the separation cell into multiple smaller cells that are bounded by the streamwise vortices and terminate in the attached flow.

I. Background

Internal flows in imposed adverse pressure gradients are highly susceptible to local, sustained flow separation leading to flow instabilities and significant energy losses. Active flow control can potentially mitigate such adverse effects by delaying separation or bypassing it altogether. Understanding the underlying flow structure of both the separating and reattaching flow has been the focus of a number of studies.

---

[1] PhD Candidate, Woodruff School of Mechanical Engineering.
[2] Senior Research Engineer, Woodruff School of Mechanical Engineering.
[3] Professor, Daniel Guggenheim School of Aerospace Engineering, AIAA Fellow.
[4] Professor, Woodruff School of Mechanical Engineering, AIAA Fellow.

Large separation domains, generally associated with post-stall aerodynamics, are highly three-dimensional, and the separated flow naturally evolves into cellular structures, or stall cells [1,2] that are characterized by two distinct surface foci. These cellular structures occur even on high aspect ratio planforms with the overall number of cells present being dependent on the aspect ratio, while the size of the individual cells seems to be independent of this parameter [1]. Weihs and Katz [1] suggest that the stall cells form due to an instability of the leading and trailing-edge vortices. Yon and Katz [3] investigated the unsteady flow within stall cells and their pressure measurements revealed high-frequency ($St \approx 0.15$) and large-amplitude low-frequency ($St \approx 0.04$) oscillations. The authors attributed the former to the wake instability, and the latter to the leading and trailing-edge shear layers interacting with the model surface, while noting the frequencies measured were much lower than anticipated by bluff body shedding and that during tuft visualization the flow remained highly unsteady on the interior of the stall cells. The global stability study by Theofilis and Rodriguez [4] attributed the formation of the cells to amplification of the global laminar separation mode leading to a three-dimensional spanwise modulation of the separation that amplifies and breaks down to form spanwise-periodic cells of separated flow regions in which the streamlines organize around two counter-rotating foci. Stereo PIV investigations by Manolesos and Voutsinas [5] on an 18% thick cambered airfoil designed for use on large scale wind turbines show that the surface-bound vortices in the separation cell are formed normal to the surface and quickly bend in the streamwise direction as they lift off the surface and are convected into the airfoil's wake as trailing vortices. Parametric studies by Dell'Orso and Amitay [6] on a NACA 0015 airfoil indicated that the cells form above a critical Reynolds number and further changes in the Reynolds number and angle of attack lead to a variety of distinct surface patterns that altered the number of cells present as well as their spanwise distribution (i.e. irregular spacing across the span). A number of investigations have focused on the receptivity of the separation cells to active perturbations. Esfahani, Webb, and Samimy [7] used plasma actuators for effecting time-periodic perturbations on a separated flow over a VR-7 airfoil and showed that increasing the actuation Strouhal number stabilizes the shape of the stall cells within a frequency band above which the separating flow ceases to respond to the actuation.

The present investigations focus on controlled reattachment of the separated flow within a finite separation cell using spanwise arrays of streamwise vortices of prescribed spanwise periodicity. For example, Johnston and Nishi [8] used vortex generating jets to form longitudinal vortices similar to those of solid vortex generators, to significantly diminish stalled regions of a flat-plate turbulent boundary layer in an adverse pressure gradient where the strength and the sense of the vortices was varied by jets' velocity ratio and skewing angle relative to the downstream direction. Otto et al. [9] compared the effectiveness of fluidically oscillating to steady jets for control of separation on a curved surface (NASA hump) and showed that for a given jet spacing, fluidically oscillating jets yielded improved control authority at lower momentum, mass, and energy coefficients as compared to steady jets. These authors argued that the improved control authority of the fluidic oscillators was associated with the spatial coherence of the induced streamwise vortices compared to the vortex array produced by the steady jets. In a related investigation of separation control using fluidically oscillating jets, Kim and Kim [10] demonstrated that the control authority is sensitive to the pitch angle of the actuation jets (relative to the surface) as the jet evolves from a normal issued jet to a wall-jet. The performance of the jets to reduce separation, as measured by the non-dimensional measure of the integral pressure compared to the baseline termed the figure of merit (FM), showed a significant decline from 0.77 at skew angles of 20 degrees to 0.39 when the jet issued normally to the surface. The pitch angle of the jet issuance also effects the structural development of the induced flow. Investigations by Namgyal and Hall [11] indicate that as the pitch angle of the control jet increases such that it forms a turbulent wall-jet , the sense of the induced counter-rotating vortex pair is switched from up- (typical of a jet issued normal to a cross-flow) to down-welling along the jet's centerline. The investigation of vortex pairs embedded in a turbulent boundary layer by Pauley and Eaton [12] showed that when the secondary flow is directed away or towards the surface, there was an associated thickening or thinning of the boundary layer that is accompanied by streamwise spreading of the vorticity without significant loss in circulation. Vortex pairs with central upwelling flow tend to be displaced from the surface, while central down-welling keeps the pair wall bound and effects streamwise lateral spreading].

The earlier work of Peterson et. al. [13, 14] showed a separating boundary layer in an adverse pressure gradient can be effectively controlled by a spanwise array of counter-rotating pairs of streamwise vorticity engendered by fluidically oscillating surface-tangential jets that are similar to the vortices that form by a wall jet in the absence of crossflow with down-welling flow along the jet centerline. The adjacent pairs of opposite-sense vortices draw low momentum fluid from the surface into concentrated regions of turbulent kinetic energy in between the jets.

The present experimental investigations build on these earlier works and focuses on the topology of the interactions between a spanwise array of fluidic actuators of varying periodicity and the flow within a separation cell that lead to reattachment with specific attention to the evolution of spanwise distributions and characteristics scales of engendered streamwise vorticity concentrations. Of particular note is the connection between instantaneous multiple strands of small-scale streamwise vorticity concentrations of alternating signs within the domain that would be occupied by the time-averaged single-sense vortices. Surface oil visualization is used to characterize the effect of the discrete actuation jets on the structure of the cell.

II. Experimental Setup and Methodology

The present investigation is performed in an open-return, small transonic wind tunnel that is operated in suction ($M < 0.75$). The square test section (Figure 1) measures 127 mm on the side and is 660 mm long. The inlet plenum is equipped with a turbulence management section upstream of a 43.56:1 contraction. The present experiments are conducted at $M = 0.25$ (the total and static pressure at the inlet as well as the air temperature are monitored).

The investigation focuses on control of a separation cell that forms in the cross flow over a nominally 2-D modular curved surface insert in the side wall of the test section. The insert models the suction surface of a VR-12 airfoil at $\alpha = 13^{\circ}$ having a chord of c = 62 mm (Figure 1) and a trip wire of diameter 0.007c that is mounted at $x/c = 4.8$ (.05c upstream of the model's leading edge). The model is fabricated using stereolithography and comprises three interchangeable segments. Flow control is effected using integrated spanwise arrays of fluidically spanwise-oscillating jets (each orifice is 1 mm wide and 0.5 mm tall) that issue tangentially to the surface of the model at 0.26 x/c downstream of the airfoil's leading edge. Three arrays are tested with actuators jet centerlines spaced $\Delta z/c$ = 0.11 ("1X"), 0.22 ("2X"), and 0.33 ("3X") with 17, 7, and 5 actuators respectively. The momentum coefficient of each jet is inferred using benchtop measurements of the jets' thrust normalized by the momentum flux through the test section and $C_{\mu jet}$ = 0, 0.02, 0.05, 0.08, and $0.12 \cdot 10^{-3}$. The jet oscillation frequency for these flow rates ranges from 6-12 kHz.

The flow within the separation cell that forms between the tunnel walls over the surface of the airfoil model is characterized using high-resolution particle image velocimetry (PIV) using a laser sheet that passes through an optical window either in a planar configuration in the cross stream plane $z = 0$ along the model's centerline, or in a stereo configuration in spanwise vertical planes (as shown in Figure 1). The PIV cameras are positioned using a computer-controlled traversing mechanism. Planar PIV measurements (200 fps) are acquired in multiple, partially-overlapping fields of view along the central plane that are integrated into a composite flow field in post-processing. Stereo PIV images are acquired at 15Hz fps at a center segment at $-0.21 < z/c < +0.21$ and $0 < y/c < 0.32$ above the local surface. In addition, the topology of the separation cell is assessed using surface oil flow visualization that is applied in either a uniform dot-matrix with spacings of 0.1c or uniformly.

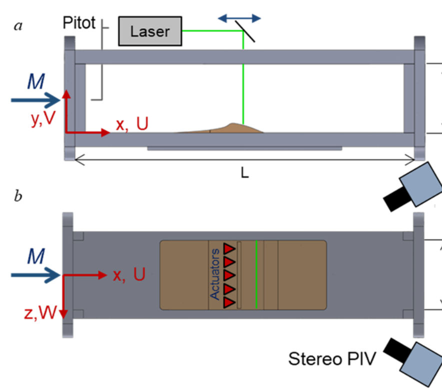

Figure 1. *Flow geometry side (a) and bottom (b) views. Stereo PIV camera locations, laser sheet alignment, and global coordinate system (x,y,z) are shown for reference.*

III. The Effects of Actuation on the Time-Averaged Flow

The topology of the separation cell that forms between the tunnels walls over the insert model is assessed using surface oil flow visualization (Figure 2a). An image of the oil flow is shown in Figure 2a, where its left edge is located at the orifices of the spanwise actuation jets (x/c = 5.1) and it spans the entire width of the test section. As shown, in the absence of actuation (M = 0.25) a single separation cell is formed in which a nominally 2-D separation domain (marked 1 in Figure 2a) is bounded by a pair of counter-rotating vortices (marked 2 and 3). The downstream end of the cell is bounded by reattachment (marked 4) and the oil streaks show evidence of upstream flow to the left of the reattachment. While the flow along the upper and lower segments is directed towards the foci of the vortices, the flow at the center shows upstream migration and significant slowdown at the center segment of the cell as indicated by the slight motion of the applied oil dots in this region. The planar PIV measurements in the cross stream plane z = 0 (Figure 2b) is a composite color raster plot colored by the mean spanwise vorticity overlaid with equidistant mean velocity vectors consisting of multiple, partially-overlapping planar PIV fields. The unactuated flow is characterized by a large-scale separating shear layer that forms at $x/c \approx 5.2$ and extends in the streamwise direction past the trailing edge of the airfoil ($x/c \approx 5.8$) until the flow is deflected toward the surface and ultimately reattaches at $x/c \approx 6.4$ although the cross stream vorticity layer remains quite wide.

Earlier investigations at Georgia Tech demonstrated the effectiveness of fluidic actuation for separation control (e.g., Peterson et. al [13] and Peterson et. al. [14]). The effect of the actuation on the separation cell are demonstrated with the spanwise 1X array with $C_{\mu\mathrm{jet}} = 0.12 \cdot 10^{-3}$ and the corresponding surface oil visualization and composite PIV measurements in the center plane z = 0 are shown in Figures 3a and b. It is immediately evident that the actuation changes the topology of the base flow cell. The near jet region (marked 1 in Figure 3a) clearly shows high speed reattached flow along the surface as is evident by the oil streaks compared to the mostly stationary oil in the same region of Figure 2a. It is notable, however, that despite the reattached flow, the foci of the bounding vortices (marked 2 and 3) are still present but appear to be significantly intensified and are displaced farther downstream and closer to each sidewall of the test section. Furthermore, while the downstream section of the cell (marked 4) is reattached, the flow along its spanwise edges is affected by the edge vortices as is evident by the oils streaks that are drawn towards the vortices. The PIV data in the center plane (Figure 3b) indicates that the flow is fully attached to the airfoil's surface but the adverse streamwise pressure gradient due to the diffuser effect of the attached flow leads to a thicker boundary layer above the bottom surface that is marked by a thicker vorticity layer.

The effect of the spanwise wavelength on the structure of the streamwise vorticity is investigated using three spanwise arrays of fluidically oscillating jets. The earlier work of Peterson et al. [14] postulated that shear effects similar to a wall jet in the absence of a cross flow are the cause of the ensuing development of time-averaged streamwise vorticity concentrations where the cross-stream and streamwise vorticity concentrations (ξ_y and ξ_x, respectively) couple and tilt downstream due to the velocity deficit near the surface. As noted, the streamwise vortices are aligned such that they result

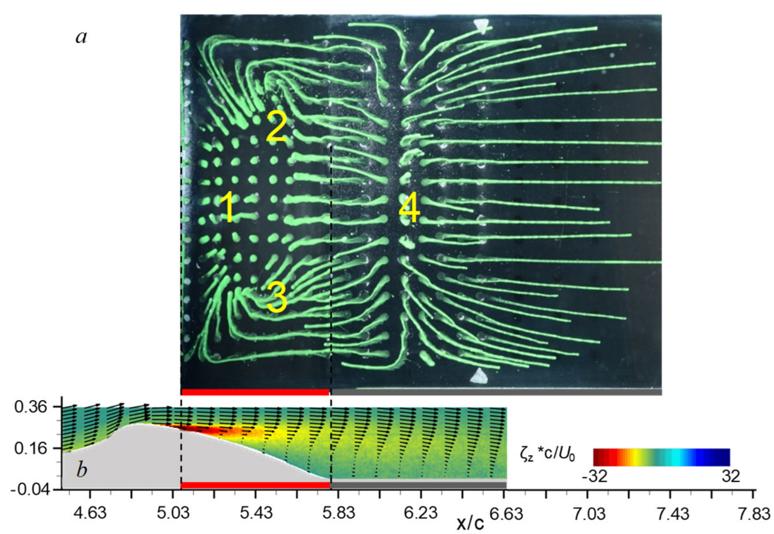

Figure 2. *Surface oil flow visualization of the separation cell in the absence of actuation (a) and color raster plots of the time-averaged vorticity overlaid with mean velocity vectors (b) at M = 0.25. The oil flow begins at the jet orifice* $\Delta x/c = 0.26$ *from the leading edge (left edge of the image in*

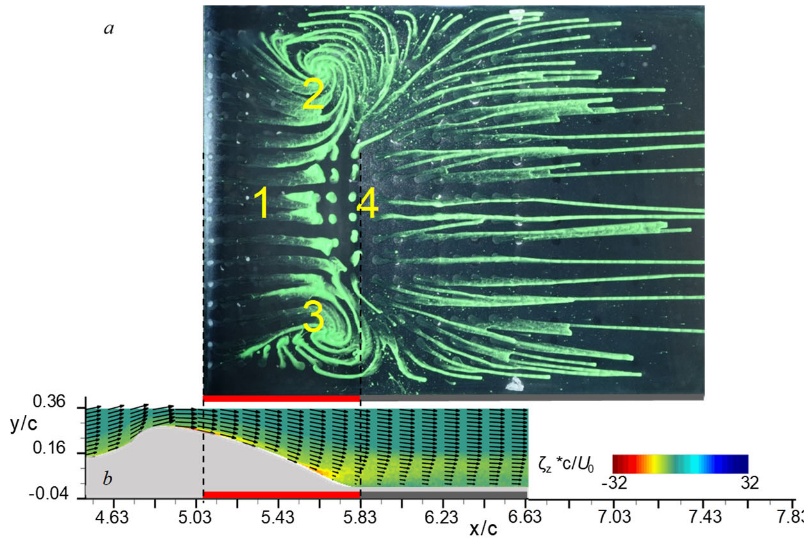

Figure 3. *As in Figure 2 in the presence of actuation with the 1X array (jet spacing 0.11c) with jet momentum coefficient $C_{\mu jet}$ = 0.12·10^{-3}. The corresponding planar PIV is shown in (b).*

in spanwise periodic alternating up- and down-welling at the center plane and between adjacent jets, respectively. The effect of the actuation jet spacing is analyzed using three spanwise arrays for which $\Delta z/c \approx 0.11$, 0.22, and 0.33, (1x, 2x and 3x, respectively), for which the center jets are aligned with the centerline of the model ($z/c = 0$). The flow of the actuation jets was characterized using a total pressure probe scanned along the span of the model *in- situ* ($\Delta z/c = 0.004$) in the absence of cross flow at $x/c = 5.1$XX where the mass flow rate of each jet was adjusted to match its thrust for $C_{\square jet} = 0.12\cdot10^{-3}$ and is shown in Figure 4. Since the scan is done *in situ,* however, the proximity of the jets in the 1x model to the wall did not capture the edge jet at $z/c = 1.02$ (the jet locations and spacing are shown schematically in Figure 4). While the total pressure distributions of individual jets within a given array are reasonably similar, there are differences between the distributions of jets from different arrays. As the jet spacing increases in the 2X and 3X arrays, the total pressure distributions exhibit nearly bimodal-like profiles that are characteristic of fluidically oscillating jets, whereas the jets of the 1X array have a single peak about the jet's centerline and elevated total pressure between neighboring jets, indicating that the denser array results in spanwise interaction of neighboring jets. These interactions diminish significantly when the spacing between the neighboring jets increases.

It is clear that the actuation has significant effect on the global topology of the flow (cf. Figure 3), which stems from significant localized effects of the jets. It was also discovered in the prior work that the 1x actuation jets form pairs of streamwise vorticity concentrations of opposing sense in the time averaged sense, with the overall sense of rotation such that there is an associated downwash region along the center of the jet, and an associated upwelling region in between the jets [14]. The proximity of the neighboring jets and the associated bounding effects have significant effect on the flow structure as well. Figure 5 shows the time averaged distributions of the streamwise vorticity (Figure 5 row a, c, e) and associated turbulent kinetic energy (Figure 5 row b, d, f) for the 1x (Figure 5, row a, b), 2x (Figure 5, row c, d), and 3x (Figure 5, row e, f) models for a single downstream plane located at $x/c = 5.72$ (a single plane is shown for brevity) and increasing $C_\mu\cdot10^3$ per jet = 0 (Figure 5, column 1) ,0.02 (Figure 5, column 2), 0.05 (Figure 5, column 3), 0.08 (Figure 5, column 4),and 0.12 (Figure 5, column 5). The triangles mark the spanwise actuator locations in the model, where only the three central jets are captured for the 1x model, while only the single centerline jet is captured in the PIV field of view for the 2x and 3x models. When examining the development

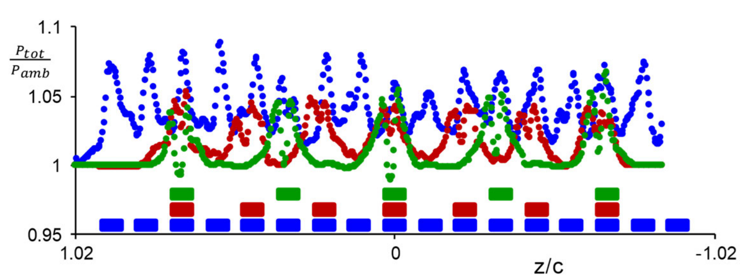

Figure 4. *Spanwise variation of total pressure measured using a miniature total pressure tube across the actuation jets at $x/c \approx 5.1$: 1x (●), 2x (●), and 3x (●) arrays. The schematic below shows the location of active jets for each array.*

of the streamwise vorticity concentrations for each model, there are general trends that are observed as the actuation is increased from the base flow (Figure 5, column 1) to the highest C_μ per jet (Figure 5, column 5). The unactuated flow shows no prevailing, coherent sense of vorticity for any models (Figure 5, column 1, row a, c, e). However, as actuation is increased, it is clear that there is a coherent, although weak at first, development of organized streamwise vorticity in the outer flow, that intensifies as it becomes drawn to the surface with the further increase in actuation. This is especially evident in the 1x and 2x models (Figure 5 row c and e respectively). The development of vorticity concentrations of opposing sense due to the actuation is also clearly shown and is strongest in the highest actuation cases for each spacing model (Figure 5, column 5, row a , c ,e). The jets form a positive, counter-clockwise vorticity concentration (colored red) to the right of the jets and an opposing, negative, clockwise vorticity concentration (blue) to the left of the jets center. This gives a rise to the combined upwash region in between the jets and an associated downwash region on the centerline of the jets. The effect of the spacing of the jets on the streamwise vorticity is clearly seen when comparing the highest C_μ cases for the three models (Figure 5, column 5, row a, c, e). Although the vorticity concentrations for each model have stretched away from the model surface due to the imposed adverse pressure gradient, the overall height of the concentrations is comparable; however, their spanwise extent is clearly altered by the jet spacings. In the 1x model (Figure 5, column 5, row a), the vorticity concentrations are closely paired together and there are multiple concentrations due to the three actuators present in the measurement domain. However, when the jet spacing is doubled (Figure 5, column 5, row c) and only one center jet is visible, the vorticity concentrations spread laterally and essentially "fill" the

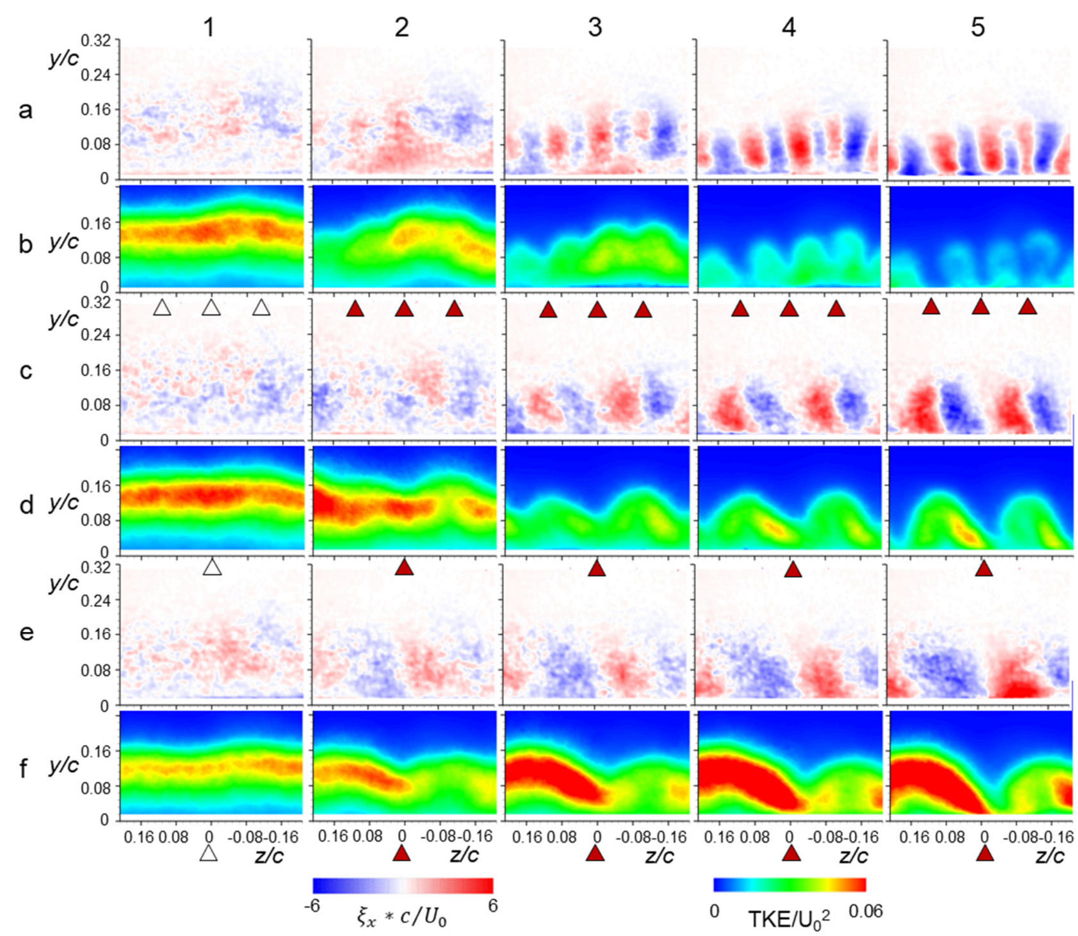

Figure 5. *Color raster plots of concentrations of streamwise vorticity (rows a, c, e) and turbulent kinetic energy (rows b, d, e) for jet arrays: 1X (row a, b), 2X (row c, d), and 3X (row e, f) in the y-z plane x/c = 5.72 for increasing* $C_{\mu jet} \cdot 10^3$ *= 0(column 1) ,0.02 (column 2), 0.05 (column 3), .08 (column 4),and 0.12 (column 5).*

empty space in between the jets in the upwash region. The vortical spanwise spreading within the dead zone between the jets is even more pronounced in the 3x model (Figure 5, column 5, row e) where only one pair of vorticity concentrations is fully captured, but the matching pairs are evident at each edge of the measurement domain, implying the same pairing structure that the 1x and 2x models have demonstrated. Consequently, the formation of the upwash and downwash regions, as well as the varying jets spacings, has implications on the turbulent fluctuations in the flow. Unlike the vorticity concentrations, the base flow (Figure 5, column 1, row b, d, e) is highlighted by a concentrated band of turbulent kinetic energy (TKE) associated with the outer shear layer of the separated flow, that stretches away from the surface in this downstream measurement plane. Similar to the vorticity concentrations, however, the effect on the TKE is clearly seen first in the outer flow. As C_μ increases, the initial concentrated band of TKE begins to be segmented and drawn to the surface for all three models (Figure 5, row b, d, f) for the 1x, 2x, and 3x models respectively). At the highest actuation level, the 1x model clearly shows a significant reduction in the peak TKE levels that were present in the unactuated flow (Figure 5, column 5, row b), while also organizing the remaining high TKE levels into concentrated regions that form halo-like structures in the regions between the jets. The 2x model also demonstrates similar behavior, in that the initially high band of TKE present is broken up and reorganized into concentrated regions that form in the dead zone between the jets (Figure 5, column 5, row d). Unlike the 1x model, however, the 2x model does not show the same reduction of the peak TKE levels, but rather only slightly reduces the highest levels. This trend continues into the 3x model (Figure 5, column 5, row f) where instead of reducing the TKE, the reorganization of the TKE into these concentrated regions between the jets has actually caused the peak levels to amplify. Once organized into the regions between the jets, it is clear the vorticity structure, namely the sense of upwelling in between the jets, also effects the structure of the TKE levels in these regions. It can most clearly be seen in the 3x model (Figure 5, column 5, row f) where the peak TKE levels are concentrated in a rounded band with the upwelling region near the model surface centered between the jets having lower levels of TKE, due to the low speed flow being drawn away from the surface. It is also clear that the proximity of neighboring actuators affects the regions of peak TKE in between the jets. As the C_μ per jet is kept constant, only the actuation wavelength across the model is changed, which leads to the expansion of the TKE (and vorticity) into these regions being defined purely by the bounding of the neighboring jets. The closest proximity of the neighboring jets imposes the most thwarted growth of the TKE region (Figure 5 column 5, row b), whereas the largest spacing (Figure 5, column 5, row f) allows the TKE to expand throughout this zone

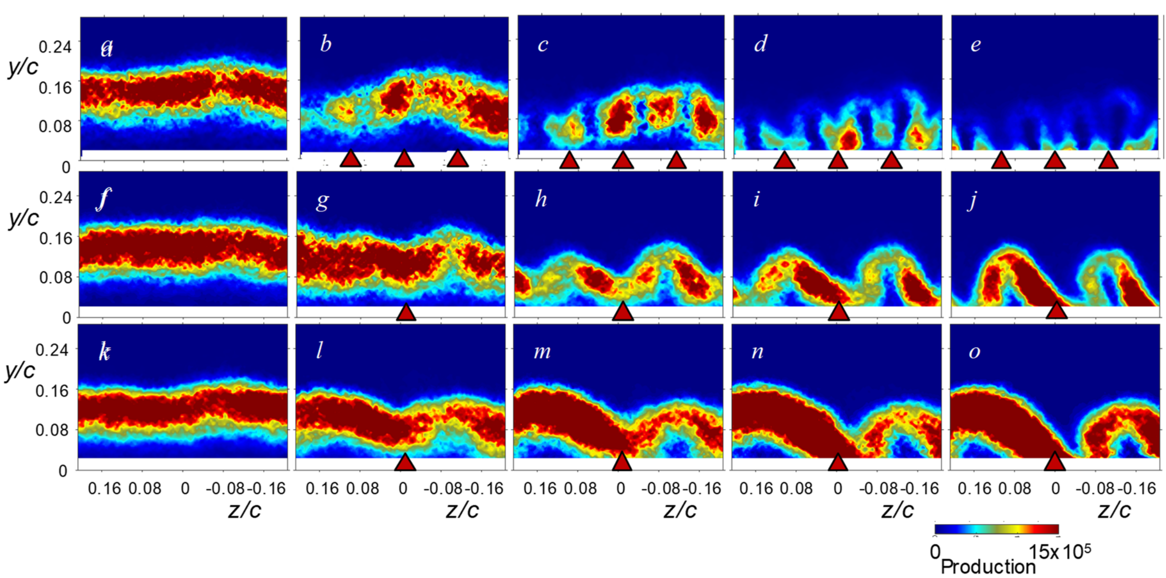

Figure 6. *Turbulent production for the 1x (a-e), 2x (f-j), and 3x (k-o) models at a single streamwise plane located at x/c = 5.72 for increasing* $C_\mu \cdot 10^3$ *per jet = 0(a,f,k,) ,0.02 (b,g,l), 0.05 (c,h,m,), .08 (d,i,n),and 0.12 (e,j,o).*

between the jets. It can be argued that relaxed spacing between the jets allows for wider interaction of each of the control jets with the oncoming flow, enhancing the mixing and TKE, while the close spacing between the neighboring jets inhibits this interaction and maintains more organized vortical structures. Even in the absence of the cross flow (Figure 4), proximity of the neighboring jets of the 1x model bounded the growth of the jets, whereas the 3x model allowed for full spreading and isolation between the jets.

The total TKE discussed in Figures 5 simply highlights the structure of the turbulent energy, and further insight is gained by examining the regions producing or dissipating the turbulent energy. The turbulent production and dissipation in the flow are shown in Figure 6 and 7, respectively, for the stereo PIV plane located at $x/c = 5.72$, and for varying actuation levels of $0 < C_\mu \cdot 10^3/\text{jet} < 0.12$. The individual terms are calculated as the following: production: $\Pi = -\langle u_i u_j \rangle \overline{S_{ij}}$ and the dissipation as: $\varepsilon = 2\nu \langle s_{ij} s_{ij} \rangle$ (Pope [15]). It is important to note the estimates associated with calculation of these parameters. As the data is taken in a single streamwise plane, the derivatives in the x-direction ($\partial/\partial x$) are excluded, except for where they can be inferred from continuity (i.e. $\partial u/\partial x$). However, it can be argued from prior results [13] that the local streamwise variation in close proximity to the stereo plane locations can be considered small as compared to the variations in other directions. Furthermore, Namgyal and Hall [11] also argue that in the far field of a turbulent wall jet, relevant for the present study, such jets also change slowly in the direction of issuance.

Just as the total TKE of the base flow, the turbulent production is also contained within the separated shear layer for the 1x, 2x, and 3x models, as shown in Figure 6 a, f, k, respectively, for the same streamwise plane at $x/c = 5.72$. As the actuation C_μ is increased, the same general trend is observed for the 1x (Figure 6a-e), 2x (Figure 6f-j), and 3x (Figure 6k-o) models, in that the initially concentrated band of turbulent production is segmented due to the jets' interaction, and then drawn towards the surface. In all models, the production levels that remain high in the actuated cases (Figure 6 e, j, o) again form halo-like structures in between the jets. In the 1x model (Figure 6e) there is a significant reduction in peak production levels, which can again be attributed to the bounding of the neighboring jets, whereas the 2x model (Figure 6j) shows only slight reduction, and finally the 3x model (Figure 6o) shows intensified production within the remaining bands; all similar trends to the already discussed effects on TKE Of note is that similar to the development of the TKE in Figure 5 with increasing C_μ ,the production levels remain high in intensified bands within the region associated with upwelling between the jets, and furthermore show areas of lower production at the center of these regions near the surface (Figure 6j and o) where the low momentum fluid is being drawn up from the surface. Following the analysis of the turbulent production, Figure 7 shows a

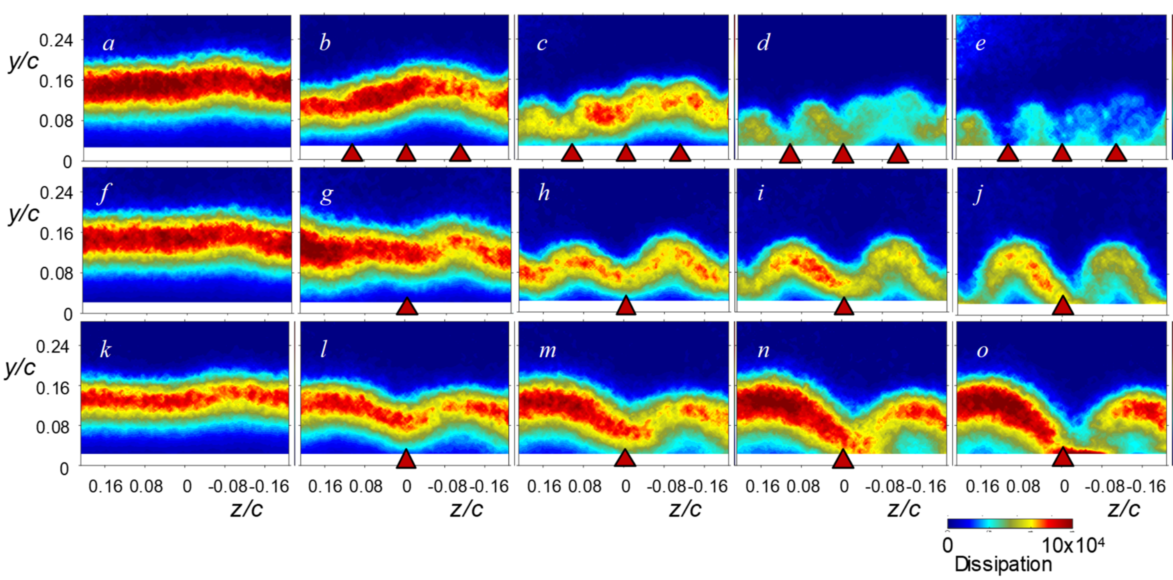

Figure 7. *Turbulent dissipation for the 1x (a-e), 2x (f-j), and 3x (k-o) models at a single streamwise plane located at x/c = 5.72 for increasing $C_\mu \cdot 10^3$ per jet = 0(a,f,k,) ,0.02 (b,g,l), 0.05 (c,h,m,), .08 (d,i,n),and 0.12 (e,j,o).*

similar analysis for the turbulent dissipation. Similar to the production levels, the onset of actuation begins to break up the initial band of the shear layer-bound turbulent dissipation and draw it to the surface. As the actuation is increased, both the 1x (Figure 7a-e) and 2x (Figure 7f-j) show consistently declining peak levels of dissipation rate, as the initial band is segmented and formed into the familiar halo-like structures. Unlike the production, however, the 1x model (Figure 7e) does not form discrete structures, but rather the remaining dissipation levels span the entirety of the space between the jets. Unlike the 1x and 2x models, the 3x model shows a reversal in the trend as C_μ is increased and shows an increase in peak levels of the dissipation, as seen in Figure 7o.

IV. Instantaneous Flow Structure

Analysis of the flow up to this point mostly focused on the time-averaged characteristics and structure of the flow. Clearly, all of the turbulent characteristics of the flow: TKE (Figure 5), turbulent production (Figure 6), and dissipation rate (Figure 7) indicate that there are significant fluctuating components of the flow, caused by the changing instantaneous flow structures, particularly in the controlled flows. To illustrate the differences, Figure 8 compares the averaged fields for the unactuated flow (Figure 8 a) and highest $C_\mu \cdot 10^3$/jet = 0.12 (Figure 8 c, e, g) to a single sample frame (Figure 8 b, d, f, h) of the instantaneous vorticity field calculated using a velocity field reconstructed with 40 modes of the velocity-based proper orthogonal decomposition (POD) for the 1x (Figure 8 a, b, c, d), 2x (Figure 8 e, f) and 3x jet spacings (Figure 8 g, h). The POD reconstruction was applied to filter out the smallest scales while preserving the dominant vorticity structures. The instantaneous flow fields (Figure 8 b, d, f, h) highlight the inherent complexity of the separated flow that cannot be seen in the time-averaged fields, although the time-averaged structures of pairs of vorticity concentrations of opposing sense are commonly referred to as 'vortices' and deemed inherent to the underlying flow reattachment. It is particularly evident when examining the unactuated flow, that the time averaged result shows no distinct organization of the streamwise vorticity (Figure 8a), but the instantaneous flow features vorticity concentrations of opposing sense interspersed throughout the separated flow region (Figure 8b). It is perhaps even more remarkable, that the regularly structured time-averaged flows are comprised of rather complex vortical interactions of different scales (Figure 8 d,

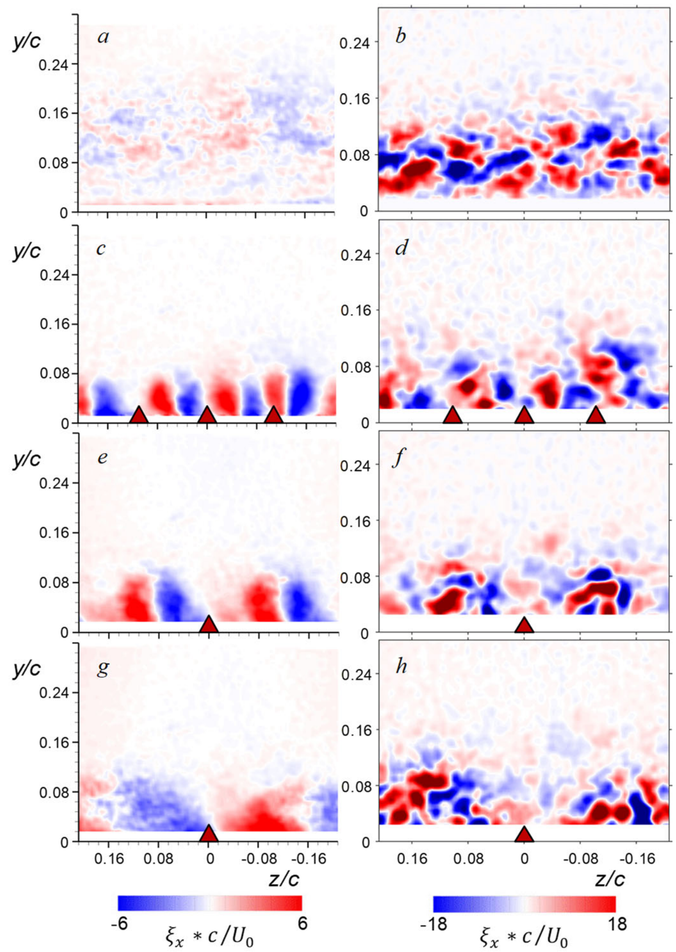

Figure 8. Time averaged (a, c, e, g) and example 40 POD mode reconstructed instantaneous (b, d, f, h) streamwise vorticity fields for the 1x (a, b, c, d), 2x (e, f), and 3x (g, h) spacing models at the streamwise plane x/c = 5.54 for the unactuated flow (a, b) and highest $C_\mu \cdot 10^3$ per jet = 0.12 (c, d, e, f, g, h).

f, h), revealing a much more complex flow structure than suggested by the time-averaged fields. For instance, the 2x (Figure 8f) and 3x (Figure 8h) actuated flows show that the interaction of the control jets and the cross flow results in clusters of vortical concentrations between the jets, while the averaged flow fields indicate the presence of a single counter-rotating vortex pair (Figure 8 e, g).

The underlying question when comparing the instantaneous and time averaged flow fields of Figure 8, is how does such a complex, time-dependent flow field result in an organized manner and structure in the time-average sense in the form of opposing vorticity concentrations? An examination of the RMS of the instantaneous streamwise vorticity fields compared to the time averaged field are shown in Figure 9 for the 1x (Figure 9 row a, b, c), 2x (Figure 9 rows d, e, f), and 3x (Figure 9 rows g, h, i) arrays for increasing $C_\mu \cdot 10^3$ per jet = 0 (Figure 9 column 1) ,0.02 (Figure 9 column 2), 0.05 (Figure 9 column 3), .08 (Figure 9 column 4), and 0.12 (Figure 9 column 5) at three streamwise planes located at x/c = 5.26 (Figure 9 rows a, d, g), 5.54 (Figure 9 rows b, e, h), and 5.72 (Figure 9 rows c, f, i). The instantaneous fields analyzed in Figure 9 are not filtered using the POD modal reconstruction. It is shown in the unactuated base flow for all three models (Figure 9 column 1) that there are large vorticity fluctuations throughout the separated shear layer, despite the time averaged flow fields showing no coherent structure. For all three models at the most upstream measurement plane at x/c = 5.26, the highest actuation levels (Figure 9 column 5, row a, d, g) show minimal differences in the RMS compared to the base flow due to the near surface proximity of the separating flow. However, the 2x (Figure 9 column 5, row d) and 3x (Figure 9 column 5, row g) show that areas of high RMS are concentrated in regions between the jets, where there is room for the vorticity to develop in the spanwise dimension, while the 1x model (Figure 9 column 5, row a) does not show the same organization of the RMS due to the bounding of the neighboring jets. Downstream, at the measurement plane x/c = 5.54, the unactuated flow RMS fluctuations have shifted away from the surface and intensified as the separated shear layer has diffused away from the surface due to the imposed adverse pressure gradient (Figure 9 column 1, row b, e, h). The effect of the actuation on

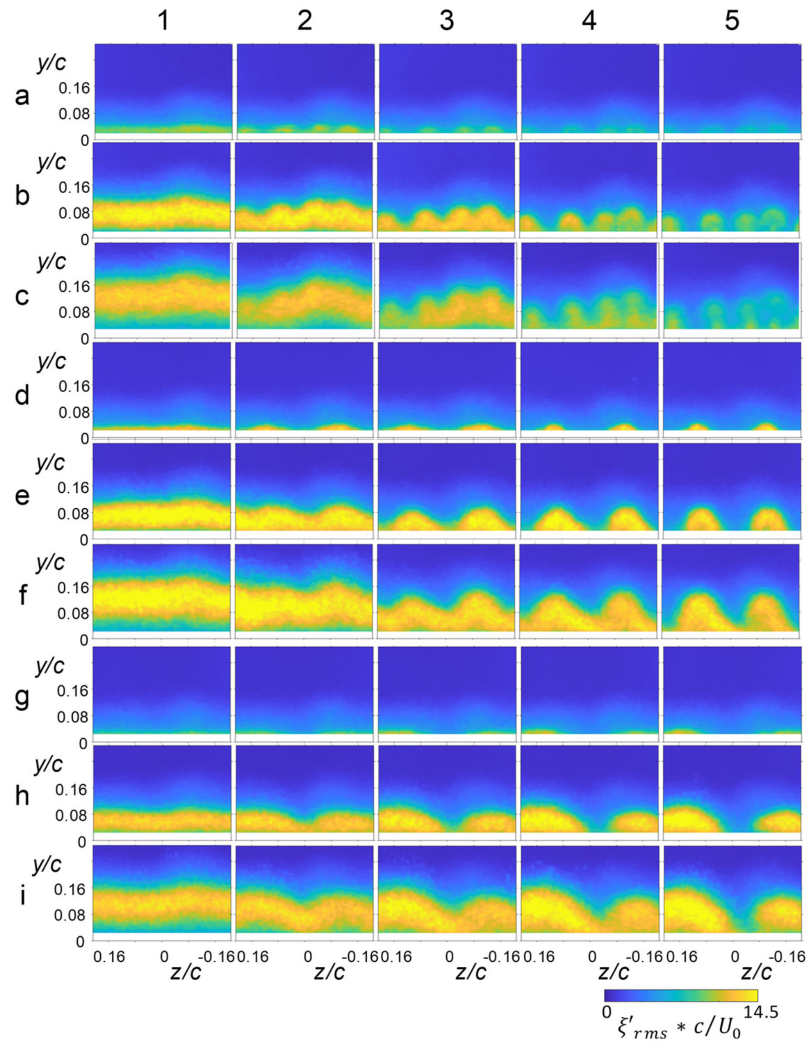

Figure 9. *Streamwise vorticity RMS for the 1x (rows a, b, c), 2x (row d, e, f), and 3x (rows g, h, i) arrays for increasing $C_\mu \cdot 10^3$ per jet = 0 (column1) ,0.02 (column 2), 0.05 (column 3), .08 (column 4),and 0.12 (column 5) at three streamwise planes located at x/c = 5.26 (row a, d, g), 5.54 (rows b, e, h) and 5.72 (rows c, f, i)*

the organization of the flow and the effect of the jet spacings can be clearly seen in this measurement plane. Following the 1x model from the unactuated flow condition to the highest $C_\mu \cdot 10^3$ per jet (Figure 9 row b), it is shown that the RMS follows closely the TKE development (Figure 5 row b), in that the initially concentrated band is segmented, drawn towards the surface, organized into structures between the jets, and diminished compared to that in the unactuated flow. This noticeable reduction in peak RMS suggests that the 1x model jets organize the flow more coherently due to the bounding of the neighboring jets and restrict the growth of vorticity in the upwelling regions. This effect persists to the farthest measurement domain (*x/c* = 5.72, Figure 9 column 5, row c) where the remaining RMS levels are concentrated into similar structures, although stretched farther away from the surface due to the imposed adverse pressure gradient. This trend changes noticeably when the jet spacing is increased. When examining the 2x model for the measurement plane at *x/c* = 5.54 from the unactuated flow condition to the highest $C_\mu \cdot 10^3$ per jet (Figure 9 row e), the familiar segmentation of the initial RMS layer is again recovered, however, with noticeable differences in the highest actuation levels when compared to the 1x model. The 2x model exhibits a growth in RMS levels in the associated upwelling region between the jets (Figure 9 column 5, row e), while having noticeably suppressed fluctuations at the center line of the jets. It appears the increased spacing of the jets allows for mild bounding effects where the vorticity develops in between the jets, but the jets themselves reduce the formation of vorticity concentrations, as evidenced by the low levels of RMS all the way to the surface of the model along the centerline of the jets at *z/c* = 0 (Figure 9 column 5, row e). This is also somewhat evident moving farther downstream (*x/c* = 5.72, Figure 9 column 5, row f), but the size of the high RMS regions has grown and the lower extent of these concentrations have encroached on the previously clear region along the centerline of the jet. Similar to the 2x model, the 3x model also shows segmentation of the initial RMS layer for both measurement planes at *x/c* = 5.54 and 5.72 with increasing actuation (Figure 9 row h, i, respectively). However, the increased spacing results in further augmentation of the RMS layer in the dead regions between the jets as the RMS concentrations fill the span between the jets while maintaining low levels of RMS along the centerline. It is clear that the jet spacing affects the flow re-organization by concentrating the development of streamwise vorticity into the upwash regions in between the jets in all three arrays.

The analysis of the vorticity RMS gives insight into the overall difference between the instantaneous flow and the time averaged structure. It does not, however, explain how the time-averaged flow fields develop into the pairs of vorticity concentrations of opposing sense (namely, a counterclockwise, positive sense to the right of the jets, and an associated negative clockwise on the left) from the complex instantaneous fields that show intermingling of vorticity of both senses within the upwelling region discussed previously in Figure 8. Figure 10 explores the composition of the flow (Figure 10 a, d, g) for the 2x spacing model at the streamwise plane located at *x/c* = 5.54 and three

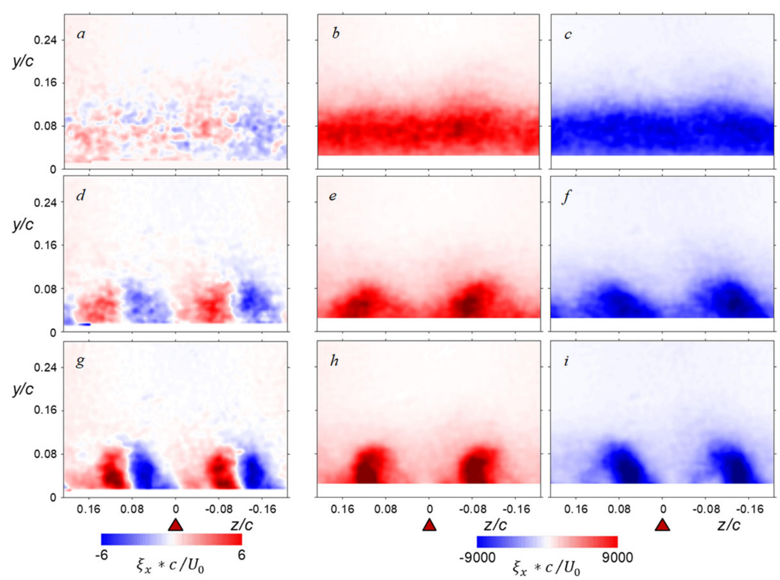

Figure 10. *Time averaged (a, d, g), cumulative positive (CCW) (b, e, h), and cumulative negative (CW) (c, f, i) thresholded streamwise vorticity for the 2x spacing model at the streamwise plane x/c = 5.54 and* $C_\mu \cdot 10^3$ *per jet = 0(a,b,c), 0.05 (d, e, f), and 0.12 (e,j,o). Jet location (z/c = 0) shown as red triangles for reference.*

actuation levels of $C_\mu \cdot 10^3$ per jet = 0 (Figure 10 a, b, c), 0.05 (Figure 10 d, e, f), and 0.12 (Figure 10 g, h, i) by thresholding the positive (Figure 10 b, e, h) and negative (Figure 10 c, f, i) vorticity concentrations and examining their cumulative concentrations. As discussed earlier, the unactuated flow (Figure 10a) shows no strong coherent vorticity structure in the time averaged flow, despite having strong bands of TKE and vorticity RMS. However, when examining the instantaneous flow, the distributions of the cumulative positive (CCW, Figure 10b) and negative (CW, Figure 10c) streamwise vorticity are shown to be interspersed throughout the separated domain, and also demonstrate no difference in magnitudes of their cumulative sums. When the actuation is applied (Figure 10d), the time-averaged structure, as discussed prior and shown here again for reference, shows a clear organization of the streamwise vorticity into two pairs of vorticity concentrations that span the region in between neighboring jets. It is evident, however, when examining the thresholded vorticity concentrations (Figure 10 e, f) that the instantaneous flow is also affected by the jets in terms of its organization. The concentrations of both positive and negative vorticity span throughout the regions between the jets, and clearly coexist despite the organized clusters in the time-average sense. Furthermore, it is shown that within these cumulative views of single sense vorticity that "hot spots" show up within these distributions (Figure 10 e and f). As the actuation is increased further (Figure 10h, i), the vorticity concentrations clearly show a preferential location to each sense, but the region between the jets is still common to both senses of vorticity. However, the peak locations, in the cumulative sense, align with their respective sense of persistent time averaged vorticity (Figure 10g). This points to preferential domains of single-sense vorticity in the cores between the jets, despite the widespread distribution, which eventually leads to the prevailing alternating clusters of single-sense vorticity in the time-average flow.

As the thresholded vorticity in Figure 10 suggests the prevalence of a single-sign vorticity concentration that persists to create the time averaged flow condition, further statistical analysis of the development and organization of these concentrations is sought. In order to examine the statistical characteristics inherent to the flow fields, three representative points are selected for each model based on the highest C_μ per jet, such that the three points are located in the core of the time averaged concentrated vorticity region immediately to the left (□), center (○), and right (△) of the central jet in each field of view, i.e., about the center of each vorticity concentration associated with a single jet and about the jet orifice. Figure 11a shows the time averaged vorticity for the 2x model at the streamwise plane x/c = 5.54 and actuated at $C_\mu \cdot 10^3$/jet = 0.12. For reference, Figure 11a also marks the points selected to examine the distributions of the streamwise vorticity within the three characteristic domains. For each individual point, a histogram of the vorticity levels is formed from the 40-POD mode reconstructed velocity fields. The vorticity histograms for the left, center, and right points are shown in Figure 11b, c, and d respectively. The histogram for the clockwise vorticity concentration to the left of the center jet (Figure 11b) is skewed to the left showing how the distribution is biased towards negative vorticity concentrations, while also highlighting that both senses are present in the same location at different instances in time. The center point distribution (Figure 11c) shows that in the centerline of the jet both senses of vorticity are present in a much narrower distribution, having

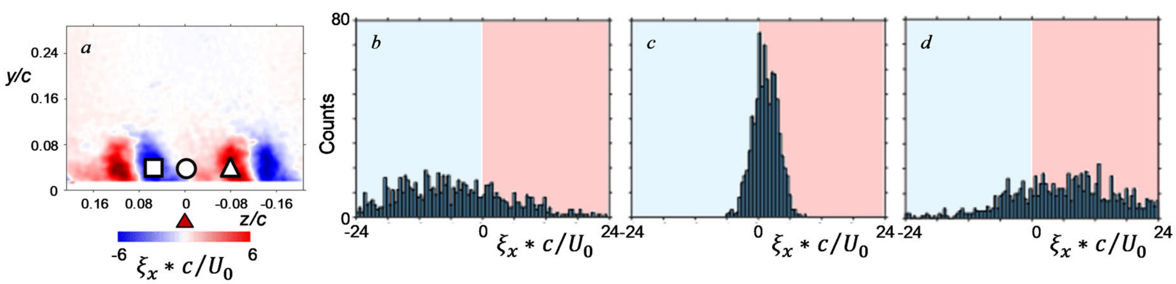

Figure 11. *Time averaged streamwise vorticity field (a) highlighting the three locations selected for the left (□), center (○), and right (△) of the jet to examine distributions of the 40 POD mode reconstructed vorticity concentrations for the 2x model at the streamwise plane x/c = 5.54 and $C_\mu \cdot 10^3$ per jet = 0.12, and the ensuing histograms of the streamwise vorticity for each selected point (left (□) b, center (○) c, and right (△) d).*

no clear preference to either sense of vorticity. The closer grouping of the vorticity distributions along the center of the jets also demonstrates the jets' imprint on the actuated flow as they redistribute the vorticity, favoring the regions on the jet outskirts, i.e., in between the neighboring jets. Finally, as it may be expected, distribution within the counter-clockwise vorticity concentration (Figure 11d) reflects the same findings observed for the clockwise side, while favoring the positive sense. It should be noted that the presented histograms are representative for each domain and that selecting a different set of points within these regions only changes the histogram distributions, but not the global features.

Figure 12 shows the mean streamwise vorticity values and the associated standard deviation for the left (□), center (○), and right (△) point locations discussed in Figure 11a for increasing actuation at three streamwise planes *x/c* = 5.26 (Figure 12 a, d), 5.54 (Figure 12 b, e), and 5.72 (Figure 12 c, f) for all three jet spacing models. As the standard deviation of the left and right points of interest show similar trends, the standard deviation (Figure 12 d, e, f) is only plotted with the center and right points of interest for brevity. The mean values in the most upstream plane (*x/c* = 5.26, Figure 12a) show the development of the streamwise vorticity for increasing actuation. When examining the center jet location (○, Figure 12a) it is clear that despite the jet spacings, the overall mean value stays near zero, indicating that in the time averaged flow there is no preferential coherent vorticity value along the centerline of the jets. However, when examining the left and right points (□ and △ symbols respectively, Figure 12a) there is a clear development of the associated signs of vorticity (negative (CW) vorticity on the first left concentration and positive (CCW) on the right) that correspond to the earlier discussion of the structure of the streamwise vorticity in Figure 5. As the actuation is increased from $C_\mu \cdot 10^3$/jet = 0 to 0.12, the magnitude of the streamwise vorticity increases while also becoming distinctly single sense in the mean. It is shown that the actuation effect becomes less pronounced by the next streamwise measurement plane downstream at *x/c* = 5.54 (Figure 12b). This can be partially attributed to the flow diffusion driven by the adverse pressure gradient. The noted trend continues to the farthest downstream plane of interest (*x/c* = 5.72, Figure 12c), where the overall spread of the vorticity concentrations is fairly contained to low absolute levels. It is interesting to note that despite the varying jet spacings, the magnitude of the time averaged streamwise vorticity remains invariant between the three arrays, even though the resulting concentrations discussed in Figure 5 were shown to have varying spanwise scale, which can be attributed to the matched jet momentum coefficient C_μ per jet. As the mean values of the vorticity concentrations at the location of interest (Figure 12a, b, c) give insight into the structure and intensity of the time averaged flow, the standard deviation (Figure 12d, e, f) is further considered as a time-dependent measure of the organization of the flow structure. At the most upstream

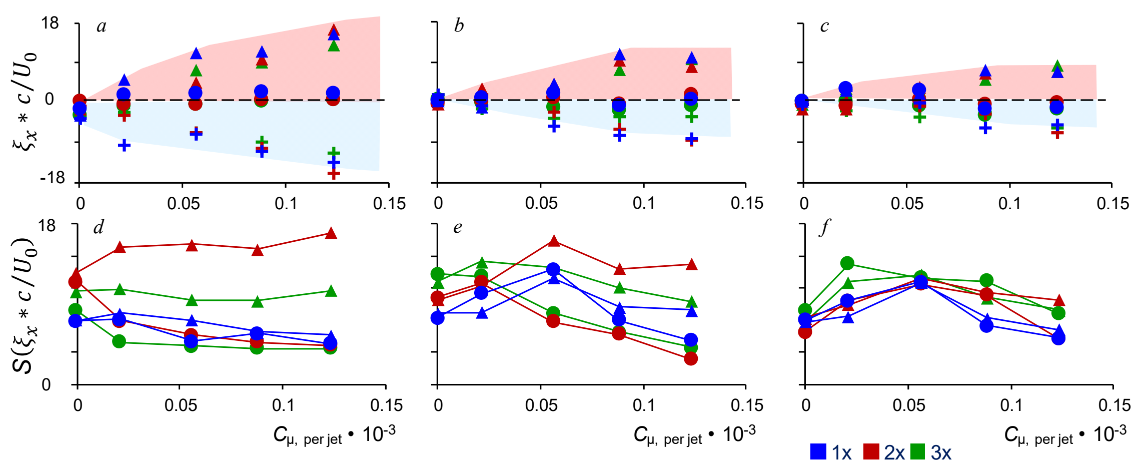

Figure 12. *Mean streamwise vorticity (a, b, c) and standard deviation (d, e, f) at the left (+), center (○), and right (△) point locations discussed in Figure 11a for increasing $C_\mu \cdot 10^3$ per jet from 0 to 0.12 at three streamwise planes x/c = 5.26 (a, d), 5.54 (b, e), and 5.72 (c, f). For the 1x (●), 2x (●), and 3x (●) models.*

measurement domain (Figure 12d) both the center and right location for the 1x model show a slight decrease in the standard deviation as the actuation is increased. The close grouping of the trends also indicates the bounding effects of the neighboring jets discussed previously. The location in between the jets thwarts the growth of the vorticity levels, and when comparing the instantaneous flow, it also appears to be more organized as the fluctuations also becomes suppressed in the 1x model. However, both the 2x and 3x models (Figure 12d) show a decrease in the standard deviation along the centerline of the jets, while showing an increase in the regions between the jets. In the larger spacing models, the absence of the bounding effect of the neighboring jets allows spanwise spreading and mixing of the jets with the outer flow, thus resulting in higher fluctuating components of the flow. The 1x model shows similar trends in the standard deviation for the jet center and neighboring reference point for both downstream measurement domains (Figure 12e and f). The data for the 2x and 3x models still highlight that the flow gets reorganized in an uneven fashion: the regions between the jets remains highly disorganized as both off-center location remains high for increasing actuation levels, while centerline values show an immediate drop in the standard deviation (Figure 12e). Interestingly, as the flow diffuses farther to the most downstream measurement plane (x/c = 5.72, Figure 12f), all three models show similar trends for the standard deviation – an initial rise and then decline as the flow control is increased. Furthermore, there is a decreased spread in the standard deviation values similar to the trend seen in the mean values discussed in Figure 12c. The variation in the standard deviation suggests that the varying jet spacings not only alter where the mean vorticity structure is created, but how the streamwise vorticity develops in the instantaneous sense.

V. Reattachment structure: separation cell effects

Analysis of the instantaneous flow characteristics focused on the underlying statistics of the vortical distributions in the controlled flow that lead to the well-defined structure of the alternating vortical concentrations in the time-averaged sense. Although each sense of vorticity appears dispersed throughout the near-surface flow, the averaged structure emerges due to increased probability of realizations of a single sense of vorticity over time in a specific area, which is in turn, also associated with predominant downwelling along the centerline of the jets and upwelling in between the neighboring jets. The ability of the jets to reattach the flow and their ensuing topological effects are further assessed in the framework of the separation cell. As stated in Section III, the base flow separation results in a single separation cell, marked by two surface foci, resulting from the three-dimensional model geometry. The actuation effect on the separation topology is demonstrated for the largest jet spacing, as the local features can be assessed with greater resolution. Hence, the oil flow visualization for the 3x model actuated at $C_\mu \cdot 10^3$ per jet = 0.12 is shown in Figure 13a with the jet locations marked by red triangles and the jet location x/c = 5.1 clearly visible, while a

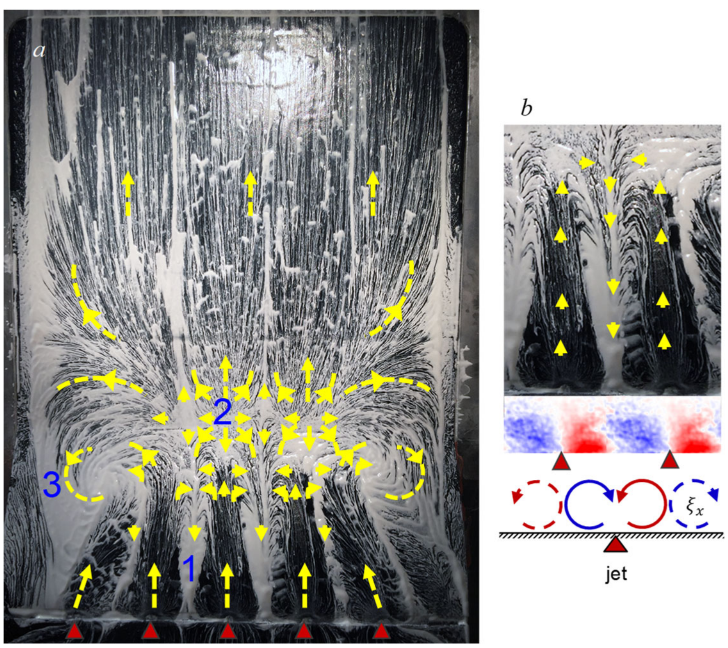

Figure 13. Surface oil flow visualization of the actuated separation cell (a) and a zoomed in view of the center and right jets with a schematic of the streamwise vorticity and sense of rotation measured in Figure 5 in respect to the jet locations (b) at M = 0.25 and for the jet momentum coefficient $C_\mu \cdot 10^3$ = 0.12 for the 3x model. Actuator locations are marked with red triangles.

zoomed in view of the center and right of center jet is shown in Figure 12b with a schematic representing the associated senses of vorticity measured at the downstream location $x/c = 5.72$. It is seen that the overall topological shape is similar to that shown in the actuated flow for the 1x model discussed previously in Figure 3; namely a presence of the remnants of the two foci that have been displaced downstream (Figure 13 region 3), as well as the smooth reattached region that moved upstream (Figure 13 region 2). Unlike the previous oil flow visualization (Figure 2 and 3), the oil was not applied in a dot-matrix pattern in order to examine fine details of the near-surface flow. Therefore, a combination of the continuous oil application and increased surface area between the jets in the 3x model assisted the oil flow visualization to highlight the structure of the individual jets and the regions between them (location 1 Figure 13). Along the center jet, the flow begins to peel off to both the left and right into the dead zones between the neighboring jets, as the flow progresses downstream. Regions of reverse flow and the associated upwellings are tied to this zone. The peeling of the jets due to the shearing effect along the center, as well as a coupling to the induced vertical shearing that gives rise to the streamwise vorticity concentrations is present in all jet spacings with increasing actuation. This coupling effect was proposed in the prior work [14] to drive the structure of the reattached flow in the 1x model. The regions of reverse flow between the jets result from the combined shearing effect between neighboring jets, where the lower momentum fluid is then pushed upward due to the associated surface pressure gradient between this region and the outer flow. This effect is highlighted in the zoomed-in view of the center jets in Figure 13b that shows the center and right jet with their associated streamwise vorticity concentrations shown schematically below. These schematics emphasize the associated upwelling between the jets and downwash region along the center of the jets. Consequently, the downwash region is associated with the reattached flow along the centerline of the jets. As this initial interaction between the control jets and the flow takes place in a nominally separated region, the resulting flow topology can be seen as piecewise-reattaching flow across the span, segmented due to the discrete jet spacing. Such a view is also reflected on the alteration of the base flow separation cell. Recall from the initial unactuated separation cell of Figure 2, that the overall shape of the cell is characterized by two u-shaped domains split along the initial reattachment line beyond which has smoothly reattached flow progressing uniformly downstream. Contrary to this base flow scenario, at the downstream end of the jets there exists multiple spanwise regions that show the same topological structure as seen in the base flow, namely two u-shaped regions pointing up and downstream. These regions can be considered as multiple, smaller, and adjacent localized separation cells that bound themselves and span across the spanwise domain. The formation of these structures suggest that the individual jets reattach the flow by dividing the initial large separation cell into multiple smaller cells, and the resulting effect due to the subdivision and shrinking of the separated domain is reattached flow along the model. This flow reattachment topology is clearly tied to the discrete array of the fluidic-oscillating jets, indicating that the eventual flow reattachment is facilitated through the control jet interaction domain characterized by the segmented separation cells. Thereby, the flow reattachment is facilitated in a highly three-dimensional fashion, even in the case where the base flow would be nominally two-dimensional.

VI. Conclusions

Control of a separation cell that forms in the cross flow over a nominally 2-D curved surface that models the suction surface of a VR-12 airfoil was investigated in wind tunnel experiments by exploiting receptivity of the cellular separated flow to unsteady actuation by spanwise arrays of tangential fluidic oscillating jets, with specific emphasis on the effects of varying actuation periodicity. The ensuing spanwise interactions between the actuation jets and the separated flow were investigated in detail within the nominally 2-D central domain of the separated flow using time-averaged and instantaneous high-resolution stereo PIV. The effects of the actuation on the global evolution of the separation cell was assessed using surface oil flow visualization.

The oil visualization shows that in the absence of actuation, the separated flow forms a single separation cell over the surface of the model that spans the full width of the test section and includes a nominally 2-D central domain bounded by two counter-rotating edge vortices that form on the surface and are advected by the cross flow. The flow reattaches downstream of the trailing edge of the airfoil model. A remarkable characteristic of the cell in the absence of actuation is the low-speed flow domain downstream from separation with weak reversed flow. The actuation jets lead to nominally 2-D central reattachment, but the edge vortices which are still present appear to intensify. Instantaneous PIV measurements in the central domain of the cell in the absence of actuation exhibit concentrations of multiple small-scale streamwise vorticity concentrations of alternating sense that appear to be randomly distributed within the flow and therefore the time-averaged flow exhibits little or no spanwise coherence. However, the spanwise periodic actuation appears to align the instantaneous streamwise vorticity concentrations with the strong shear domain between the jets although the corresponding spanwise periodic populations still include multiple strands of clockwise and counterclockwise streamwise vortices. The time-averaged flow, however, exhibits a spanwise periodic array of streamwise vorticity concentrations of alternating sense that are aligned with the actuation jets and seemingly are associated with time-averaged, spanwise periodic down- and up-welling of fluid along the jets centerline and between adjacent jets, respectively. This statistical organization of the flow is indicative of the effects of the shear associated with the actuation jets. The actuation wavelength affects the characteristic cross stream scale and spanwise periodicity of the time-averaged streamwise vorticity concentrations. The organized up-welling of the flow between the actuation jets leads to spanwise-periodic concentrations of turbulent kinetic energy which is more limited as the spacing between the jest decreases, indicating that the actuation effectiveness can be significantly diminished by dense actuation arrays owing to spanwise interactions.

The flow control's effect on the global topology of the separation cell is assessed using surface oil visualization. The actuation jets appear to segment the cell into smaller spanwise-periodic cellular structures that are each bounded by a pair of counter-rotating streamwise vortices. These effects persist when the actuation wavelength is increased. These observations indicate that there are topological similarities between the large-scale cell and the individual, segmented cells which enable the reattachment of the flow farther upstream than in the global cell.

Acknowledgments

Funding provided by the Georgia Tech Vertical Lift Research Center of Excellence is gratefully acknowledged.

References

[1] Weihs, D., and Katz, J., "Cellular Patterns in Poststall Flow over Unswept Wings," *AIAA Journal*, Vol. 21, No. 12, 1983, pp. 1757–1759. doi:10.2514/3.8321

[2] Schewe, G.,"Reynolds-number effects in flow around more-or-less bluff bodies," *J. Wind Eng. Ind. Aerodyn*. 89, 2001, pp. 1267-1289.

[3] Yon, S.A., and Katz, J., "Study of the unsteady flow features on a stalled wing," *AIAA J.,* Vol 36, No. 3,1998, pp. 305-312.

[4] Rodriguez, D. and Theofilis, V., "On the birth of stall cells on airfoils," *Theor. Comput. Fluid Dyn*. 25(1–4), 105–117 (2010).

[5] Manolesos, M., and Voutsinas, S. G., "Study of a Stall Cell Using Stereo Particle Image Velocimetry," *Physics of Fluids*, Vol. 26, No. 4, 2014, Paper 045101. doi:10.1063/1.4869726

[6] Dell'Orso, H., and Amitay, M., "Parametric investigation of stall cell formation on a NACA 0015 Airfoil," *AIAA J*. Vol. 56, No. 8, 2018. https ://doi.org/10.2514/1.J056850.

[7] Esfahani, A., Webb, N., and Samimy, M., "Stall cell formation over a post-stall airfoil: effects of active perturbations using plasma actuators," *Exp. in Fluids*, Vol 59 No. 132, 2018. doi: https://doi.org/10.1007/s00348-018-2588-y.

[8] Johnston, J.P., Nishi, M., J.K., "Vortex Generator Jets – Means for Flow Separation Control," *AIAA Journal*, Vol 28 No. 6, pp. 989-994, 1990.

[9] Otto, C., Tewes, P., Little, J. C., and Woszidlo, R., "Comparison of Fluidic Oscillators and Steady Jets for Separation Control on a Wall-Mounted Hump," *AIAA Paper 2018-1281*, 2018.

[10] Kim, S., Kim, K., "Effects of Installation Conditions of Fluidic Oscillators on Control of Flow Separation," *AIAA Journal*, 2019.

[11] Namgyal, L., Hall, J.W., "Reynolds stress distribution and turbulence generated secondary flow in the turbulent three-dimensional wall jet," *J. Fluid Mechanics*, 800, pp. 613-644, 2016.
[12] Pauley, W., Eaton, J.K., "Experimental Study of the Development of Longitudinal Vortex Pairs Embedded in a Turbulent Boundary Layer," *AIAA Journal*, Vol 26, pp. 816-823, 1988.
[13] Peterson, C.J., Vukasinovic, B., and Glezer. A., "Control of a Closed Separation Domain in Adverse Pressure Gradient Over a Curved Surface," AIAA Paper 2019-1900, 2019.
[14] Peterson, C.J., Vukasinovic, B., Smith, M.J., and Glezer. A., "Controlled Attachment of a Separated Boundary Layer in an Adverse Pressure Gradient Over a Curved Surface," AIAA Paper 2020-2950, 2020.
[15] Pope, S. B., "Turbulent Flows," Cambridge University Press, Cambridge, 2000.